

Ambipolar acoustic transport in silicon

A. D. Barros,^{1,2,3} P. D. Batista,^{1,4} A. Tahraoui,¹ J. A. Diniz,^{2,5} and P. V. Santos^{1,a)}

¹Paul-Drude-Institut für Festkörperelektronik, Hausvogteiplatz 5–7, D-10117 Berlin, Germany

²School of Electrical and Computer Engineering, University of Campinas, P. O. Box 6101, 13083-970 Campinas-SP, Brazil

³Center for Semiconductor Components, University of Campinas, P. O. Box 6061, 13083-870 Campinas-SP, Brazil

⁴Centro Brasileiro de Pesquisas Físicas, Rua Dr. Xavier Sigaud, 150, 22290-180 Rio de Janeiro, Brazil

⁵Center for Semiconductor Components, University of Campinas, P. O. Box 6061, 13083-870 Campinas-SP, Brazil

(Received 19 April 2012; accepted 4 June 2012; published online 10 July 2012)

We have investigated the ambipolar transport of electrons and holes by electrically generated surface acoustic waves (SAWs) on silicon wafers coated with a piezoelectric ZnO film. The transport experiments were carried out by using a focused laser beam to optically excite carriers. The carriers are then captured by the moving SAW piezoelectric field and then transported towards a lateral p-i-n junction, where they are electrically detected. The piezoelectric modulation modifies the current vs. voltage characteristics of the lateral p-i-n junction. This behavior is accounted for by a simple model for the change of the junction potential by the SAW fields. We demonstrate that electrons and holes can be acoustically transported over distances approaching 100 μm , the transport efficiency being limited by the low mobility of holes in the material. These results open the way for silicon-based acousto-electric devices using ambipolar transport such as photo-detectors and solar cells. © 2012 American Institute of Physics. [<http://dx.doi.org/10.1063/1.4733966>]

I. INTRODUCTION

Surface acoustic waves (SAWs) are mechanical vibrations propagating on the surface of a material. From the technological point of view, these waves are particularly interesting in piezoelectric materials, where the SAW strain field is accompanied by a piezoelectric potential Φ_{SAW} . As a consequence, SAWs with frequencies up to several GHz can be electrically generated via the inverse piezoelectric effect using interdigital transducers (IDTs) deposited on the sample surface.^{1,2} The piezoelectric generation of SAWs in piezoelectric insulators such as LiNbO₃ and quartz forms the basis for their application in signal processing and acousto-optic modulation.

SAWs can also be generated electrically in piezoelectric semiconductors such as gallium arsenide (GaAs), zinc oxide (ZnO), and aluminum nitride (AlN). The spatial modulation of the refractive index of a semiconductor by the SAW strain field has been exploited in different concepts for acousto-optic modulators.^{3,4} In these materials, the piezoelectric field induces a moving type-II modulation of the conduction (CB) and valence band (VB) edges, as illustrated in Fig. 1(a). Electrons and holes photogenerated within the SAW field can be captured in spatially separated regions, thereby increasing the recombination lifetime. The trapped carriers can then be transported along the SAW propagation direction x by the moving field.^{5,6} The efficient confinement and transport of carriers by a SAW requires that the carriers are sufficiently mobile to follow the SAW field as it propagates with velocity v_{SAW} . This condition can be stated as $\mu_i \left| \frac{\partial \Phi_{\text{SAW}}}{\partial x} \right| > v_{\text{SAW}}$, where μ_i (i = electron, hole) denotes the

carrier mobility and v_{SAW} the SAW propagation velocity. The acoustic transport in semiconductors has been explored for the realization of single-electron pumps⁷ and optical switches.^{4,8–10} The acoustic transport has also been proposed for devices in quantum communication, where it can be used to transport and manipulate spins^{11,12} and to generate¹³ and detect^{14–16} single photons.

The lack of piezoelectricity in group-IV semiconductors hinders the electric generation of SAWs via the inverse piezoelectric effect. Moving piezoelectric fields can nevertheless be coupled to a silicon crystal by placing it in close proximity (i.e., within an acoustic wavelength λ_{SAW}) to a second crystal surface sustaining a piezoelectric SAW. This process has been used to achieve the piezoelectric transport of electrons in silicon (see, e.g., Ref. 17). Alternatively, SAWs can be electrically generated in group-IV semiconductors by coating the crystal with a piezoelectric thin film. The acoustic transport of electrons in monolithic Si samples coated with a piezoelectric ZnO film has also been reported (see Ref. 18).

Previous acoustic transport experiment has been restricted to the transport of electrons. In this paper, we will investigate the unipolar acoustic transport of photoexcited electrons and holes in silicon, as well as its suitability for photon detection using the acousto-electric approach illustrated in Fig. 1(b).¹⁴ In this approach, electrons and holes are created via the absorption of the incoming photons within the propagation path of a SAW. The carriers are captured by the moving SAW piezoelectric potential [cf. Fig. 1(a)] and then transported to a lateral p-i-n junction, where they are collected and electrically detected using an electrometer. The acousto-electric detection of photoexcited carriers using a similar approach has been demonstrated in

^{a)}santos@pdi-berlin.de.

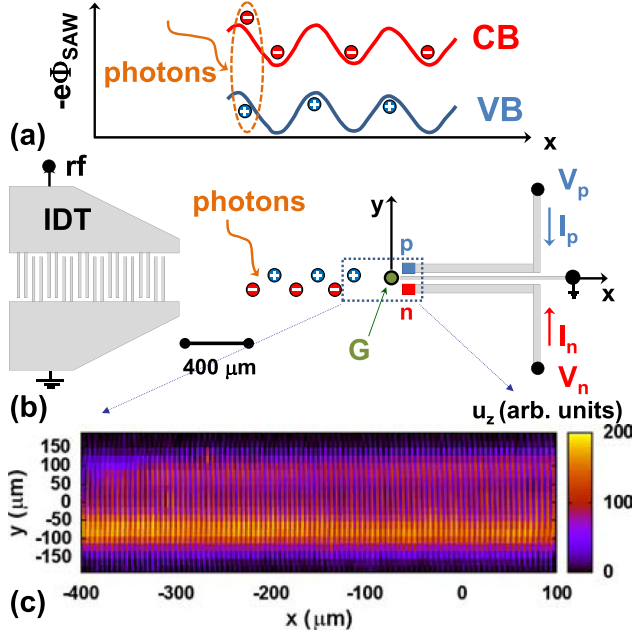


FIG. 1. (a) Modulation of the conduction (CB) and valence (VB) edges of a semiconductor by the piezoelectric potential Φ_{SAW} induced by a SAW. (b) Schematic diagram of the silicon photon detector based on acoustic transport. Electron and holes photogenerated by a light spot focused on the SAW path (spot G) are captured at the minima and maxima of the electronic energy $-e\Phi_{\text{SAW}}$ and transported towards the lateral p-i-n junction, where they are collected and detected using an electrometer. (c) Spatial distribution of the SAW field in the area indicated by the dotted rectangle in (b), recorded by mapping the amplitude u_z of the vertical component of the SAW displacement using a scanning Michelson interferometer.

(Al,Ga)As-based structures.^{16,19} Furthermore, Talyanskii *et al.*¹⁴ have shown that single-photon sensitivity with photon-number discrimination can be achieved if single-electron transistors are used to detect the transported carriers. As in Ref. 18, the acousto-electric silicon detector employs a piezoelectric film to enable electric SAW generation as well as for the piezoelectric carrier transport. In contrast to the previous acoustic transport studies in silicon, which were restricted to the unipolar electron transport, the acousto-electric photon detectors require the ambipolar transport of electrons and holes. The latter is relevant for photo-detector and solar energy conversion concepts based on the acoustic transport.²⁰

In the following sections, we first describe the steps for the fabrication of the silicon structures for acoustic transport as well as the procedures for their characterization (Sec. II). The propagation properties of SAWs in these structures as well as the spatial distribution of the acoustic and piezoelectric fields are then discussed in Sec. III A. The effects of the acoustic modulation on the current (I_{pn}) \times voltage (V_{pn}) characteristics of the lateral p-i-n junction are addressed in Sec. III B. The latter is followed by a detailed study of the ambipolar transport of electrons and holes presented in Sec. III C. Finally, the main conclusions are summarized in Sec. IV.

II. EXPERIMENTAL DETAILS

The samples were fabricated on the (001) surface of high resistivity (5 k Ω cm) floating zone silicon wafers with a

diameter of 2 in. The first fabrication steps started with the formation of the lateral p-i-n junction via the implantation of boron (50 keV; dosis of $5 \times 10^{15} \text{ cm}^{-2}$) and phosphorus (80 keV; dosis of $7 \times 10^{15} \text{ cm}^{-2}$), respectively. The depth of the n- and p-type implanted regions was 0.7 μm and 1.0 μm , respectively. A thermal oxide with a thickness of 100 nm was then formed on the sample surface at a temperature of 1000 $^{\circ}\text{C}$. As in conventional CMOS devices, the quality of the SiO₂/Si interface is essential for the operation of the devices, since the piezoelectric field attracts both electrons and holes towards this interface, where the acoustic transport takes place. The piezoelectric ZnO film (500 nm thick) was then sputtered on the sample surface at 300 $^{\circ}\text{C}$. The sputtering conditions were chosen to produce highly c-axis oriented films, which are required for good piezoelectric properties. The ZnO and SiO₂ films were patterned to allow the deposition of metal contacts on the doped areas. The IDTs were fabricated using a lift-off metalization process defined by contact photolithography yielding minimum feature sizes of approximately 0.5 μm . The metalization layer consists of a Ti/Al/Ti layer stack with thicknesses of 10 nm/40 nm/10 nm.

The IDTs were designed for an acoustic wavelength $\lambda_{\text{SAW}} = 5.6 \mu\text{m}$, corresponding to a Rayleigh SAW resonance frequency of approximately 750 MHz. The IDTs are of the single-finger type with an aperture of 300 μm and a length of 1000 μm .

The electro-optical measurements were carried out at room temperatures (RT) using a probe station with contact probes for dc and rf measurements. Experiments were also performed at lower temperatures (down to 100 K) by placing the sample in a microscope cryostat with appropriate rf-connections for SAW excitation. The n and p contacts in Fig. 1(b) were biased with voltages $V_p = -V_n = V_{pn}/2$. As a result of this symmetric bias arrangement, the currents become $I_p = -I_n = I_{pn}$. We have verified that this current relation was satisfied under all experiment conditions.

For the electro-optical measurements, the sample was illuminated using a microscopic spot (diameter of approximately 5 μm) produced by focusing a laser beam (wavelength of 532 nm at RT and 808 nm at 100 K) on the sample surface using a microscope connected to the probe station. Unless otherwise specified, the laser spot was placed at the position $G = (x, y) = (0, 0) \mu\text{m}$ indicated in Fig. 1(b) corresponding to the left edge of the grounded metal stripe placed between the contacts. This stripe was introduced in order to laterally separate the flows of photo-excited holes and electrons when they approach the junction. Note that the reference coordinate $x = 0$ is close to the left edge of the p and n contacts.

III. RESULTS

A. Distribution of the SAW fields

The scattering (s) parameters describing the rf-response of the IDTs on silicon were measured using a network analyzer. Figure 2(a) displays the rf power reflection coefficient s_{11} , which is characterized by a dip at 750 MHz indicative of SAW excitation. From the amplitude of the dip, we determined that approximately 14.4% of the input rf-power is

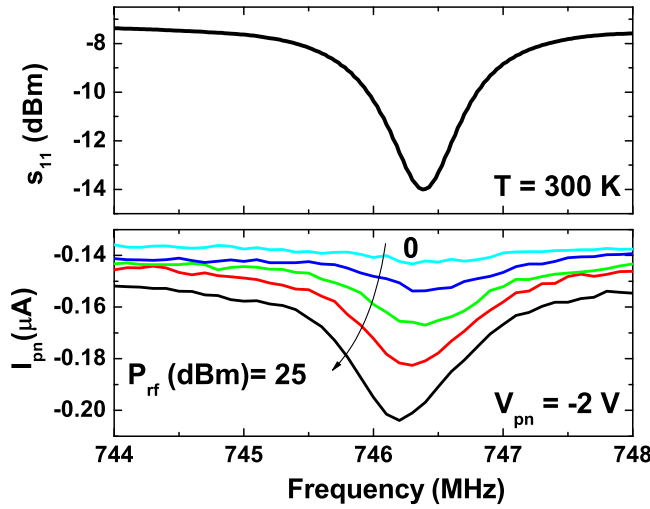


FIG. 2. Frequency dependence of the (a) s_{11} power reflection coefficient of the IDT and of (b) the junction current I_{pn} measured for different acoustic powers P_{rf} under a reverse bias $V_{pn} = -2$ V to the p-i-n junction. P_{rf} was varied from 0 dBm to 25 dBm in steps of 5 dBm. The measurements were carried out at RT using an illumination spot with an intensity of $90 \mu\text{W}$ placed in the position marked as G in Fig. 1(b).

converted into two acoustic modes propagating towards the left and right of the IDT.

The previously determined value for the electro-acoustic conversion efficiency yields directly the SAW power density P_ℓ , defined as the ratio between the acoustic power and the width of the SAW beam. P_ℓ was used to determine the amplitude of the longitudinal piezoelectric field F_x as well as the piezoelectric potential Φ_{SAW} generated by the SAW in the silicon substrate by using an elastic numerical model for the structure.⁴ Figure 3 displays depth profiles for these quantities calculated for a nominal rf-power of 23 dBm applied to the IDT (corresponding to $P_\ell = 76 \text{ W/m}$). The calculations were carried out for a free ZnO surface as well as for a sample surface coated with a thin metal layer. As will be discussed in Sec. III C 2, the latter results are important to understand acoustic transport underneath the metal bar between the n and p contacts [cf. Fig. 1(b)]. For the free surface, F_x decreases with depth z

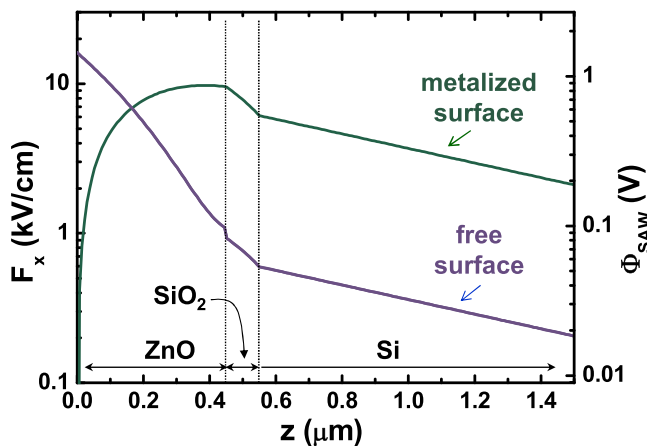


FIG. 3. Calculated depth dependence of the longitudinal piezoelectric field F_x (left scale) and piezoelectric potential Φ_{SAW} (right scale) under a SAW with linear power density of $P_\ell = 76 \text{ W/m}$.

and reaches a value of 0.56 kV/cm at the SiO_2/Si interface, where the acoustic transport takes place. By using the SAW velocity of 4243 m/s determined from the measured resonance frequency (cf. Fig. 2) and the acoustic wavelength, one obtains a minimum mobility for efficient transport of $730 \text{ cm}^2/(\text{Vs})$. This value is smaller than the intrinsic electron mobility in Si at room temperature [$\mu_e(300 \text{ K}) = 1500 \text{ cm}^2/(\text{Vs})$] but substantially higher than the hole mobility [$\mu_h(300 \text{ K}) = 450 \text{ cm}^2/(\text{Vs})$].²¹ Note that due to the high temperature oxidation step, the mobilities in the present samples are expected to be lower than these intrinsic values.

Figure 1(b) shows that the region in-between the n- and p-doped contacts was partially covered by an electrically grounded metal layer. The metal film short circuits the piezoelectric potential at the interface with the ZnO layer and changes its depth profile, as indicated in Fig. 3. Interestingly, the piezoelectric potential at the SiO_2/Si interface underneath increases by almost an order of magnitude in comparison to the values at the free surface. Similar results have been reported for GaAs layers coated with a metal film.²² As a result of the stronger fields, a high carrier transport efficiency is expected underneath the metal stripe in-between the n and p contacts shown in Fig. 1(b).

In order to measure the spatial distribution of the SAW fields on the sample surface, we used a scanning Michelson interferometer⁴ to probe the amplitude u_z of the vertical displacement field induced by the SAW. Figure 1(c) displays the distribution of u_z within the region of the acousto-electric detector indicated by the dotted rectangle in Fig. 1(a). These measurements detect the SAW field for a particular SAW phase. The closely spaced vertical lines separated by one acoustic wavelength correspond to the maxima of u_z for this particular phase. Note that the acoustic amplitude remains almost constant with increasing distance from the IDT, thus indicating negligible SAW absorption.

B. SAW effects on the p-i-n junction current

The solid lines in Fig. 4(a) displays the $I_{pn} \times V_{pn}$ characteristics of the lateral p-i-n junction recorded at 100 K for

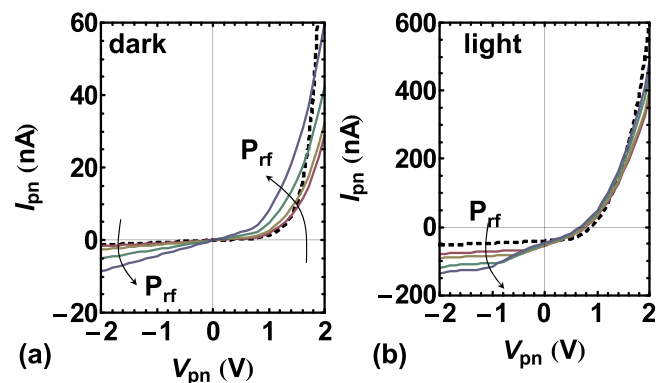


FIG. 4. Current (I_{pn}) vs. voltage (V_{pn}) traces for the lateral p-i-n junction recorded at 100 K (a) in the dark and (b) under illumination. The dashed lines were measured in the absence of a SAW. The solid traces were recorded under SAWs excited by applying rf-powers P_{rf} equal to 16, 19, 22, and 25 dBm to the IDT. The illumination spot (with light intensity $P_\ell = 6.2 \mu\text{W}$) was placed at the position G indicated in Fig. 1(b).

different rf-powers (P_{rf}) applied to the IDT. The dashed line shows, for comparison, the diode-like traces recorded in the absence of acoustic excitation. The slow onset of the forward current with applied voltage is due to the high series resistance of the lateral p-i-n junction, where the p and n regions are separated by a $40\ \mu\text{m}$ intrinsic region. In addition, the metal stripe between the two contacts screens the field between them, thereby reducing the voltage that can be applied between the intrinsic regions.

For reverse and low forward biases, the main effect of the SAW is to reduce the effective shunt resistance of the junction. The latter mainly arises from carrier injection into the Si through pinholes in the ZnO and SiO₂ films underneath the IDT, when it is subjected to a large rf-voltage, followed by transport to the p-i-n-junction. To confirm this behavior, we also applied the rf voltage to the IDT through a bias tee, which permits the simultaneous measurement of the dc current between the IDT electrodes and the p-i-n junction.

In the following, we address the $I_{pn} \times V_{pn}$ characteristics for positive voltages, where I_{pn} increases with the acoustic power. As will be discussed in the following, this behavior can be accounted for by the modulation of the diode voltage by the SAW piezoelectric field. The current increase may also have a contribution from thermal loading induced by high rf powers (see discussion in Sec. III C 2 related to the RT results of Fig. 2). The two contributions add to each other and are difficult to separate experimentally. To minimize thermal effects, we will concentrate on results obtained at 100 K (as in Fig. 4)), where thermal effects were found to be much less pronounced due to the higher thermal conductivity of silicon (the Si thermal conductivity increases by a factor of approximately 6 between 300 and 100 K).

The acoustic modulation in the structure of Fig. 1(b) creates channels of high and low piezoelectric potential between the *n* and *p* junction contacts. The spatial separation $\lambda_{\text{SAW}}/2$ between these channels is much smaller than the extension of the contacts along the SAW propagation direction. We will assume that the net effect of this potential modulation is to add a time-dependent contribution $V_{\text{SAW}}\cos(2\pi f_{\text{SAW}}t)$ to the junction voltage V_{pn} . The average junction current under this periodic voltage modulation can be obtained by inserting the previous expression for the voltage into the diode equation and integrating over one SAW oscillation period. The time-averaged junction current I_{pn} at a temperature *T* then becomes

$$I_{pn}(V_{pn}) = I_0 \left[\mathcal{I}_0(V_{\text{SAW}}/V_T) e^{\frac{V_{pn}}{V_T}} - 1 \right] - I_L. \quad (1)$$

In these expressions, $V_T = nk_B T/e$, *n* is the ideality factor of the junction, I_0 its reverse current, and I_L the short-circuit current. k_B and *e* denote Boltzmann constant and the electron charge, respectively. The modulation voltage V_{SAW} enters in the argument of \mathcal{I}_0 , which is the zeroth-order modified Bessel functions (also known as the hyperbolic Bessel function) of the first kind. Since $\mathcal{I}_0(0) = 1$, Eq. (1) reduces to the conventional diode equation when $V_{\text{SAW}} = 0$. In order to get a better insight into the effects of the modulation, the Bessel function in Eq. (1) can be expanded in power series

of V_{SAW}/V_T . For $V_{\text{SAW}} < 2V_T$, we obtain in this way the following approximation of the average pn-current:

$$I_{pn}(V_{pn}) \approx I_0 \left[e^{\frac{V_{pn} + \Delta V_{\text{SAW}}}{V_T}} - 1 \right] - I_L, \quad (2)$$

where

$$\Delta V_{\text{SAW}} \approx V_T \left[\left(\frac{V_{\text{SAW}}}{2V_T} \right)^2 - \frac{1}{4} \left(\frac{V_{\text{SAW}}}{2V_T} \right)^4 \right]. \quad (3)$$

To a first approximation, the effects of the sinusoidal SAW modulation on the non-linear *I* vs. *V* characteristics of the junction is, therefore, to add a positive contribution ΔV_{SAW} to the contact voltage.

In order to check the validity of the previous approximation, we replotted in Fig. 5 the data set from Fig. 4(a) after (i) subtraction of the contribution linear in V_{pn} due to current injection from the IDT and (ii) normalization by a factor given by

$$r_N(P_{\text{rf}}) = \mathcal{I}_0(V_{\text{SAW}}(P_{\text{rf}})/V_T) / \mathcal{I}_0(V_{\text{SAW}}(20\ \text{dBm})/V_T),$$

where the denominator corresponds to the current for a reference P_{rf} (chosen to be $P_{\text{rf}} = 20\ \text{dBm}$). For $I_{pn} \gg I_0$, this factor corrects for the current increase due to the SAW modulation. In the normalization, the acoustic modulation voltage $V_{\text{SAW}}(P_{\text{rf}})$ was assumed to be proportional to the amplitude of the SAW fields and, therefore, to $\sqrt{P_{\text{rf}}}$. In agreement with the model leading to Eq. (1), all current traces, which span an order of magnitude in acoustic powers, collapse to a single curve. The $V_{\text{SAW}}(P_{\text{rf}})$ values used for the normalization are displayed in the inset: the modulation voltages of a few tens of meV are comparable to the amplitude

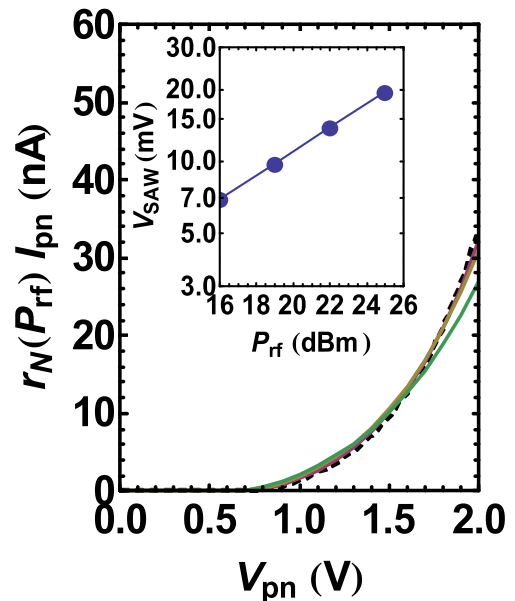


FIG. 5. $I_{pn} \times V_{pn}$ traces of Fig. 4(a) normalized by the factor $r_N(P_{\text{rf}}) = \mathcal{I}_0(V_{\text{SAW}}(P_{\text{rf}})/V_T) / \mathcal{I}_0(V_{\text{SAW}}(20\ \text{dBm})/V_T)$. The inset displays the values of V_{SAW} (on a logarithmic scale) as a function of P_{rf} (in dBm, also a logarithmic scale) used for normalization. In this log-log plot, the points fall on a straight line due to the square root dependence $V_{\text{SAW}} \propto \sqrt{P_{\text{rf}}}$.

of the piezoelectric potential at the SiO₂/Si interface displayed in Fig. 3.

The simultaneous effects of illumination and acoustic excitation on the $I_{pn} \times V_{pn}$ characteristics are illustrated in Fig. 4(b). Note, in particular, that the application of a SAW leads to an increase in magnitude of the reverse current. As will be shown in Sec. III C, the current enhancement is due to the acoustic transport of photoexcited carriers to the p-i-n junction.

C. Ambipolar acoustic transport

1. rf-frequency dependence

Figure 2 compares the s_{11} spectrum with the detected photocurrent I_{pn} measured for different SAW powers. For low P_{rf} (< 0 dBm), the current is determined by the diffusion and drift of photoexcited carriers to the space-charge area of the p-i-n junction, with no effects from the SAW. For higher P_{rf} , in contrast, the piezoelectric potential becomes sufficiently strong to capture and transport the carriers towards the junction, leading to an increase in $|I_{pn}|$. The similar frequency dependencies of s_{11} and I_{pn} give direct evidence for the ambipolar transport of electrons and holes. Note that the position of the dip in I_{pn} for $P_{rf} < 20$ dBm agrees very well with the one for s_{11} . The slight shift towards lower frequencies observed for stronger SAW is attributed to the temperature increase induced by the high applied rf-powers, which shifts the resonance to lower frequencies.

A close analysis of Fig. 2 indicates that high rf-power levels affect the amplitude of I_{pn} under illumination not only within the frequency range of the SAW resonance dip but also outside of it. This frequency independent background current is attributed to the previously mentioned injection of carriers by the rf-field applied to the IDT.

2. Dependence on acoustic power

Figure 6(a) displays the dependence of the junction current I_{pn} on P_{rf} for different junction bias voltages V_{pn} at 100 K, respectively. The position of the illumination spot is indicated by G in Fig. 1(b). Each curve shows three regions: for low acoustic powers ($P_{rf} < 0$ dBm), I_{pn} does not depend on the SAW amplitude and is determined by carrier drift and diffusion to the space charge region of the lateral p-i-n junction. For moderate powers ($0 < P_{rf} < 20$ dBm), the SAW piezoelectric potential becomes strong enough to transport the photo-excited carriers, leading to an increase in I_{pn} . Finally, for large P_{rf} values (> 20 dBm), the current reaches a maximum and then reduces with a further increase in acoustic power. The current reduction has two contributions. The first is the modulation of the junction potential (cf. Sec. III B), which adds a small positive contribution to the junction voltage. The second and more important arises from the fact that the piezoelectric field at high SAW intensities becomes sufficiently strong to prevent the collection of the transported carriers by the p-i-n junction. Note, in particular, that the transport across the intrinsic region of the p-i-n junction takes place underneath the metal bar [cf. Fig. 1(b)], where SAW piezoelectric field is more intense (cf. Fig. 3). The strong fields can, in fact, extract carriers from the p-i-n

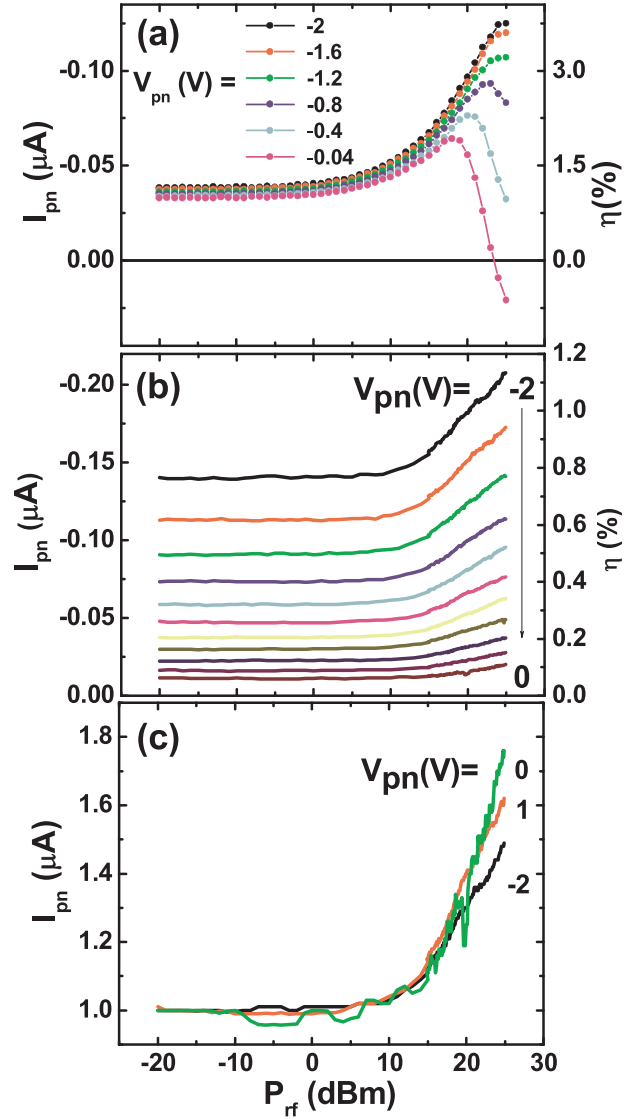


FIG. 6. Dependence of the junction current I_{pn} on the nominal rf-power P_{rf} applied to the IDT measured for different junction biases V_{pn} at (a) 100 K and (b) 300 K. The right vertical scale displays the internal quantum efficiency η calculated using Eq. (4). (c) Curves for $V_{pn} = 0, -1$, and -2 V at 300 K normalized to their corresponding values for low acoustic powers $P_{rf} < -10$ dBm. The illumination conditions were the same as in Fig. 2.

junction and transport them along the SAW path. This behavior was corroborated by experiments (not shown) carried out in structures containing a second p-i-n junction downstream on the SAW path.

In order to quantify the transport efficiency, the right vertical scale displays the internal photon collection efficiency η . For a given illumination position, η is defined as the ratio between the number (per unit time) of detected electron-hole pairs $N_{e,h}$ and the one of incident photons flux N_{ph} according to

$$\eta = \frac{1}{1-R} \frac{\hbar\omega_L}{e} \frac{\Delta I_{pn}}{P_\ell}, \quad (4)$$

where $\hbar\omega_L$ is the photon energy, P_ℓ the incident light intensity, and R is the optical reflectivity of the sample at the laser wavelength. R was calculated from the optical properties of the layers to be 60%. The maximum collection efficiency of

12% (at 100 K) was measured when the carriers are photo-generated very close to the p-doped contacts. The low efficiency is due to the large extent of the intrinsic region between the p and n contacts of the junction. The application of a SAW considerably increases the collection efficiency. For the illumination conditions of Fig. 6(a), where the carriers are generated away from the contacts, η increases with P_{rf} from the minimum value of 1% in the absence of a SAW (i.e., for very low P_{rf}) to a maximum approximately 3.5%.

Figure 6(b) displays the dependence of I_{pn} on P_{rf} measured at RT. As in Fig. 6(a), the carrier collection increases for P_{rf} values exceeding 10 dBm. In contrast to the low temperature measurements, the background current levels for low P_{rf} increase substantially with applied bias. In addition, the efficiency η is less than 2% and a reduction of the current for high P_{rf} was not observed. In order to better evaluate the effects of the SAW, Fig. 6(c) displays the curves for $V_{pn} = 0, -1$, and -2 V normalized to their corresponding values for low acoustic powers. Note that the threshold power levels for transport are independent of the applied bias. In addition, the application of a SAW enhances η by up to 80%.

3. Transport efficiency

The results presented until now were obtained by photo-exciting carriers using a laser spot at the fixed position marked

by G in Fig. 1(b). In order to obtain information about the transport efficiency, we carried out measurements of the junction current as a function of the position of the illumination spot. Results obtained in the absence of acoustic excitation and under a SAW excited by $P_{\text{rf}} = 25$ dBm are displayed in the contour maps of Figs. 7(a) and 7(b), respectively. In agreement with Fig. 6, the collected current increases substantially under acoustic excitation. The most interesting feature, however, is the asymmetric distribution of the collected current, which is much higher when carriers are generated close to the p-doped contact. This asymmetric distribution, which is also observed under acoustic excitation [cf. Fig. 7(b)], occurs despite the symmetric arrangement of the p and n contacts with respect to the SAW beam illustrated in Fig. 1(b).

Figure 7(c) displays the SAW contribution ΔI_{pn} to the collected current, which was obtained from the difference between the profiles in Figs. 7(a) and 7(b). The asymmetric current distribution is also observed in this plot. The ambipolar transport requires the collection of equal number of electrons and holes by the n - and p -type contacts, respectively. We assign the asymmetry to the lower mobility of holes as compared to electrons. As a result, holes can only be efficiently collected if generated close to the p -contact, leading to higher collection at these positions.

The acoustic transport distances can be obtained from the decay of the I_{pn} profiles of Fig. 7(c) as one moves away

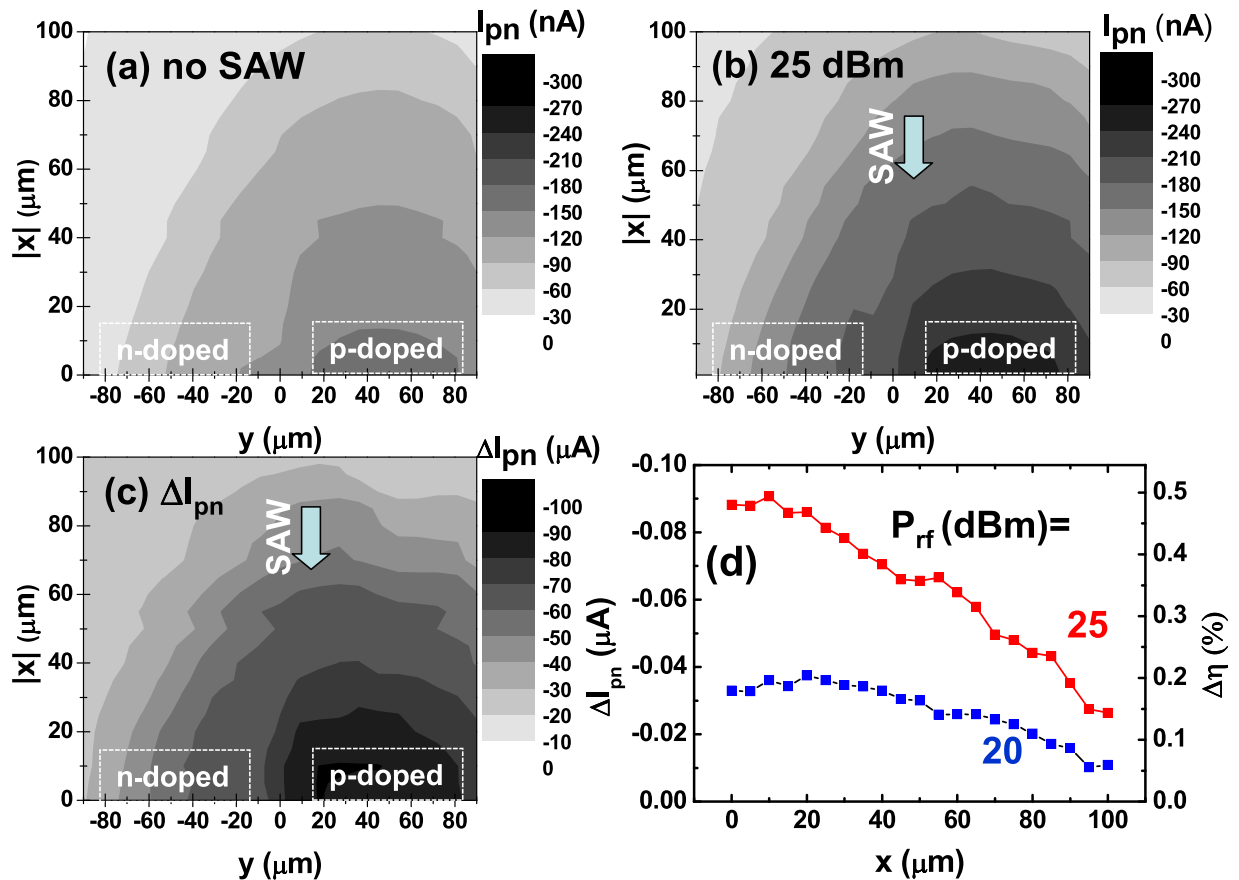


FIG. 7. Dependence of the junction current I_{pn} on the spatial position (x, y) of the illumination spot [cf. Fig. 1(a)] recorded (a) in the absence of a SAW and (b) under a SAW with $P_{\text{rf}} = 25$ dBm. (c) SAW-induced photocurrent ΔI_{pn} determined from the difference between the currents I_{pn} in plots (b) and (a). (d) Dependence of ΔI_{pn} measured at $y = 40$ μm on the distance x . The right scale displays the enhancement $\Delta\eta$ in internal collection efficiency induced by the SAW. The measurements were carried out at RT using a laser spot with 90 μW and a bias $V_{pn} = -2$ V.

from the p-doped contact. Figure 7(d) displays results obtained along the line $y = 40 \text{ } \mu\text{m}$ (corresponding to central position of the p-type contact) for two acoustic powers. The right vertical scale shows the efficiency enhancement $\Delta\eta$ induced by the SAW field. As expected, ΔI_{pn} reduces with the transport distance $|x|$. If we define the characteristic transport length ℓ as the distance to reduce ΔI_{pn} by a factor of 2.7, we obtain $\ell \approx 100 \text{ } \mu\text{m}$ for the highest acoustic power in Fig. 7(d).

The relatively short transport lengths are consistent with the field estimations of Fig. 3, which show that the maximum values of the piezoelectric potential is not sufficiently high to effectively confine electrons and holes at the minima of the acoustic modulation [cf. Fig. 1(a)]. Under these conditions, the carriers are dragged by the SAW at effective velocities much lower than the SAW propagation velocity.²³ The asymmetric distribution of the collection efficiency in Fig. 7 indicates that the transport length is mainly limited by the low hole mobility.

IV. CONCLUSIONS

We have investigated the transport of photoexcited electrons and holes by SAWs on a Si wafer coated with a SiO_2 film and with a piezoelectric ZnO film. The experiments were carried out by using a laser beam to generate electrons and holes and a lateral p-i-n junction for electrical carrier detection. The SAW piezoelectric field modulates the $I_{pn} \times V_{pn}$ characteristics of the lateral p-i-n junction: the effects of the modulation are taken into account by a simple model for the time averaged junction current. The SAW can transport the carriers over a hundred of μm , the transport efficiency being limited by the low hole mobility in the material. These results open the way for the use of acoustic fields for carrier manipulation in CMOS chips.

ACKNOWLEDGMENTS

We thank P. Bruski and A. Violante for comments and discussions as well as J. Godoy Fo, S. Krauß, S. Rauwerdink, B. Drescher, and W. Seidel for the sample fabrication. We

also acknowledge the support from the German DAAD and BMBF (“KMU-innovativ” Programm) as well as from the Brazilian CAPES.

- ¹R. M. White and F. W. Vollmer, *Appl. Phys. Lett.* **7**, 314 (1965).
- ²R. M. White, in *Proceedings of the IEEE* (IEEE, New York, 1970), Vol. 58, p. 1238.
- ³A. Korpel, *Acousto-Optics* (Marcel Dekker, Inc., New York, 1997).
- ⁴M. M. de Lima, Jr., and P. V. Santos, *Rep. Prog. Phys.* **68**, 1639 (2005).
- ⁵M. J. Hoskins, H. Morkoç, and B. J. Hunsinger, *Appl. Phys. Lett.* **41**, 332 (1982).
- ⁶C. Rocke, S. Zimmermann, A. Wixforth, J. P. Kotthaus, G. Böhm, and G. Weimann, *Phys. Rev. Lett.* **78**, 4099 (1997).
- ⁷J. M. Shilton, V. I. Talyanskii, M. Pepper, D. A. Ritchie, J. E. F. Frost, C. J. B. Ford, C. G. Smith, and G. A. C. Jones, *J. Phys.: Condens. Matter* **8**, L531 (1996).
- ⁸F. Alsina, J. A. H. Stotz, R. Hey, and P. V. Santos, *Solid State Commun.* **129**, 453 (2004).
- ⁹M. M. de Lima, Jr., R. Hey, and P. V. Santos, *Appl. Phys. Lett.* **83**, 2997 (2003).
- ¹⁰M. M. de Lima, Jr., R. Hey, J. A. H. Stotz, and P. V. Santos, *Appl. Phys. Lett.* **84**, 2569 (2004).
- ¹¹J. A. H. Stotz, R. Hey, P. V. Santos, and K. H. Ploog, *Nature Mater.* **4**, 585 (2005).
- ¹²O. D. D. Couto, Jr., F. Iikawa, J. Rudolph, R. Hey, and P. V. Santos, *Phys. Rev. Lett.* **98**, 036603 (2007).
- ¹³O. D. D. Couto, Jr., S. Lazić, F. Iikawa, J. Stotz, R. Hey, and P. V. Santos, *Nat. Photonics* **3**, 645 (2009).
- ¹⁴V. I. Talyanskii, G. J. Milburn, J. A. H. Stotz, and P. V. Santos, *Semicond. Sci. Technol.* **22**, 209 (2007).
- ¹⁵M. van der Poel, M. Beck, M. B. Dühring, M. M. de Lima, Jr., L. H. Frandsen, C. Peucheret, O. Sigmund, U. Jahn, J. M. Hvam, and P. V. Santos, *Proceedings of European Conference on Integrated Optics and Technical Exhibition, Copenhagen, Denmark, 25–27 April 2007* (unpublished).
- ¹⁶P. D. Batista, R. Hey, and P. V. Santos, *Appl. Phys. Lett.* **93**, 262108 (2008).
- ¹⁷S. D. Gaalema, R. J. Schwartz, and R. L. Gunshor, *Appl. Phys. Lett.* **29**, 82 (1976).
- ¹⁸K. Tsubouchi, T. Higuchi, M. Nagao, and N. Mikoshiba, *Appl. Phys. Lett.* **33**, 762 (1978).
- ¹⁹S. J. Jiao, P. D. Batista, K. Biermann, R. Hey, and P. V. Santos, *J. Appl. Phys.* **106**, 053708 (2009).
- ²⁰V. M. Yakovenko, *Physica B* **407**, 1969 (2012).
- ²¹*Landolt-Börnstein Tables*, edited by O. Madelung (Springer Verlag, Heidelberg, 1982), Vol. 17a.
- ²²K. Biermann, O. D. D. Couto, Jr., W. Seidel, R. Hey, and P. V. Santos, *Appl. Phys. Lett.* **96**, 162106 (2010).
- ²³A. García-Cristóbal, A. Cantarero, F. Alsina, and P. V. Santos, *Phys. Rev. B* **69**, 205301 (2004).